Behavior analysis of comb-drive actuators operating in near-zero-overlap configuration

A. Marković, H. Fanet, G. Pillonnet, B. Legrand

Sensors & Actuators: A. Physical 376 (2024) 115652

Contents lists available at ScienceDirect

Sensors and Actuators: A. Physical

journal homepage: www.journals.elsevier.com/sensors-and-actuators-a-physical

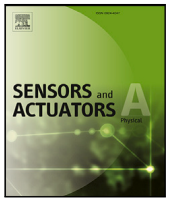

Behavior analysis of comb-drive actuators operating in near-zero-overlap configuration

A. Marković [a,*], H. Fanet [b], G. Pillonnet [b], B. Legrand [a]

[a] LAAS-CNRS, Univ. Toulouse, Toulouse, 31400, France
[b] CEA-Leti, Univ. Grenoble Alpes, Grenoble, 38054, France

ARTICLE INFO

Keywords:
MEMS
Comb-drive
Near-zero overlap
Fringing fields
Spring softening

ABSTRACT

Comb structures are widely used in micro-electromechanical systems as basic components of electrostatic actuators, capacitive sensors, resonators and energy harvesters. Typically, they are operated with a large overlap of the comb fingers, in the linear region. Here we study the behavior of comb-drive actuators during the displacement along the axis of the fingers in the unconventional regime where the fingers are slightly overlapping (around the width d of the fingers), which has recently gained attention in the MEMS community. In the intermediate region where the overlap approaches zero, fringing electric fields induce a non-linear variation of the capacitance, yielding a significant electrostatic force between the combs even without finger overlap with a maximum gradient occurring in this region. The comb capacitance variation with overlap was calculated using analytical and FEM modeling and confirmed with experimental results. We explored the implications of this condition in both static and dynamic modes, highlighting the effect of spring softening arising from the second derivative of the capacitance. These findings introduce new operational possibilities for actuators and sensors and substantial tunability in frequency for resonators.

1. Introduction

Micro-electromechanical systems (MEMS) have revolutionized the landscape of modern technology, enabling the development of compact, low-cost, high-performance devices [1]. Among the MEMS basic components, comb structures have played a significant role, finding extensive utilization in actuators, switches, resonant devices and sensors [2–4]. Comb-drive actuators derive their name from their comb-like structure, featuring interdigitated fingers and a movable shuttle. The principle of actuation is rooted in the capacitive attractive force between the charged comb fingers, caused by the applied voltage, which results in a linear displacement of the shuttle along the axis of the fingers. Their unique characteristics, including high precision, large stroke, absence of hysteresis and low power consumption, have established them as indispensable tools for MEMS design [5,6]. These attributes have allowed applications such as precision positioning, micro-mirror actuation, or manipulation using micro-tweezers [7–9]. Additionally, their integration into resonators and sensors schemes has led to applications in the field of mass, force and inertial sensing [10] and energy harvesting [11]. Traditionally set up with a significant overlap of the fingers, usually spanning half of their length, these actuators maintain a near-constant force under a given voltage, irrespective of the shuttle's displacement [4,12,13]. This characteristic stems from the linear variation of the capacitance within the comb structure as a function of the overlap. In contrast to this conventional configuration, we present here an investigation of the regime where the overlap of the fingers is close to zero as used recently in MEMS-based logic circuits [14] based on capacitive adiabatic logic introduced in [15]. In this case, the dominance of fringing electric fields results in a distinctly non-linear variation of the capacitance with the shuttle displacement and could be exploited in the future for increasing the sensitivity of MEMS components in this particular unconventional regime. Recently, the near-zero-overlap configuration of the comb structures has also been studied within the scope of energy harvesting [11], whereby an empirical analytical law has been proposed for describing the capacitance variation of a two-sided MEMS structure. In our device of interest, the capacitance variation, with respect to the resting position, is not symmetrical. We have therefore developed an analytical model for calculating the capacitance of comb-drive structures in this regime, based on our previous work [16]. Its accuracy was subsequently compared with the Finite Element Method (FEM) analyses which was further taken as the most exact device description and later confirmed by experimental results. All these investigations shed light on the influence of the second derivative of the capacitance. This effect plays a crucial

* Corresponding author.
E-mail addresses: markovicvaleksandra@gmail.com, amarkovic@laas.fr (A. Marković).

https://doi.org/10.1016/j.sna.2024.115652
Received 26 January 2024; Received in revised form 17 May 2024; Accepted 25 June 2024
Available online 3 July 2024

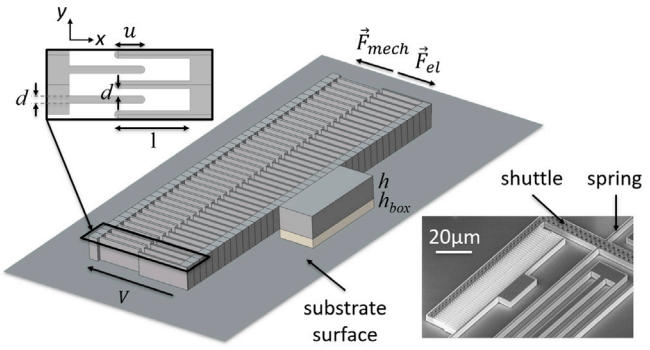

Fig. 1. Schematic of a comb-drive actuator used for FEM modeling with h being the thickness of the device, h_{box} the thickness of buried oxide, l the length of the fingers, d their width as well as the gap between them and u being the overlap between the combs. The structure is suspended above a silicon substrate, grounded in the simulations. Fingers are modeled rounded, as this form represents better the shape of the fingers after microfabrication. Inset: SEM image of a fabricated comb-drive; movable comb is connected to a spring over a shuttle.

Table 1
The basic components used in Electric Field Decomposition (EFD) approach in describing the capacitance between two electrodes.

Capacitance type	Schematic	Formula
Plate capacitance	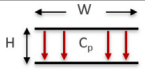	$\frac{C'_p}{\epsilon} = \frac{W}{H}$
Terminal capacitance	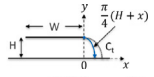	$\frac{C'_t}{\epsilon} = \frac{4}{\pi}\ln 2$
Fringe capacitance	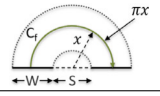	$\frac{C'_f}{\epsilon} = \frac{1}{\pi}\ln\left(1+\frac{2W}{S}\right)$

role in the behavior of comb-drive actuators operating within the near-zero-overlap regime.

2. Modeling - analytical and FEM

Our analytical model employs formulas based on Electric Field Decomposition (EFD), which were proposed in [17,18]. These formulas break down the components of capacitance, considering the effects of fringing electric fields, in order to provide an accurate representation of the system without relying on fitting parameters (see the basic components in Table 1). Principles like "field shielding" and "charge sharing" are also introduced in [17] to describe complex geometric configurations. When applying the EFD approach to model the comb structure depicted in Fig. 1, we divided the capacitance in 14 elementary components. Note that for simplicity in calculations, we assumed here a square shape for the finger tips. The capacitance calculation includes three main contributions: C_v, which depends on the degree of overlap and is formed within the comb-drive structure, C_{fix}, arising from the fixed electrode and the substrate, which remains constant across the whole range of overlap, and non-linear contributions, C_{nl}, such as those from fringing electric fields (details of the three contributions are provided in the supplementary material).

The physical and geometrical parameters used for modeling are indicated in Table 2. The choice of finger gap and width (d) was dictated by the achievable critical dimensions in terms of lithography and etching. In the common configuration of most comb-drive structures the gap equals the finger width. The dashed line plotted in Fig. 2a represents the capacitance value of the comb-drive structure based on this analytical model.

In the region where the overlap is highly negative, the calculated capacitance value remains relatively constant. Here, it is primarily

Table 2
Parameters of the comb structure used in simulations.

Parameter	Description	Value	Unit
E	Young's modulus of silicon	170	GPa
ϵ_0	Vacuum permittivity	$8.854 \cdot 10^{-12}$	F/m
ϵ_r	Relative permittivity of silicon oxide	4.2	
h	Thickness of the silicon layer	5	μm
h_{box}	Thickness of the oxide layer	2	μm
l	Length of the fingers	10	μm
d	Finger width and gap	0.5	μm
N	Number of fingers in the comb	60	

determined by the capacitance formed between the polarized fixed electrode and the grounded substrate. An approximation of this capacitance can be obtained using the formula:

$$C_{fix} = \frac{\epsilon_0(S_{comb} + \epsilon_r S_{fix})}{h_{box}} + C_{par} \tag{1}$$

Where S_{comb} is the surface area occupied by the combs and S_{fix} is the surface area of the fixation. C_{par} designates parasitic contributions like fringe and terminal capacitances that are independent of the overlap (see details in supplementary material). As the overlap between the comb fingers approaches zero, the fringing electric fields start contributing significantly to the capacitance. When the overlap becomes positive, the capacitance increases rapidly, with the dominant factor being the capacitance formed between the interdigitated fingers. This capacitance augmentation is linearly dependent on the overlap and can be described by the well known formula:

$$C_v(u) = 2N\epsilon_0\frac{uh}{d} \tag{2}$$

Where N is the number of fingers in a single comb electrode and u is the overlap (Fig. 1).

To assess the accuracy of our analysis, we conducted Finite Element Method (FEM) modeling using COMSOL Multiphysics software. We used the same set of parameters as in Table 2 to calculate the capacitance of the comb-drive structure. The movable electrode and the substrate were connected to ground, while the fixed electrode was subjected to a voltage V. We varied the initial overlap between the combs from -10 times the finger width (denoted as d) to $10d$, with steps of $1d$. Additionally, we employed smaller steps of $0.2d$ within the range of $-5d$ to $3d$. This allowed us to explore the influence of overlap with a fine analysis in the near-zero-overlap regime. We extracted the capacitance value between the grounded parts and the polarized electrode (circles in Fig. 2a). From these discrete FEM data, we then established a continuous function that describes how capacitance changes with overlap u (red line in Fig. 2a). To achieve this, we used a cubic Hermite spline interpolator [19] to fit the discrete FEM data in Fig. 2a. This approach ensured that both the fitting function and its derivative were continuous (Refer to Appendix A). As depicted in Fig. 2a, our analytical model is in a fairly good agreement with the FEM model. Nevertheless, the analytical description of the region of interest (near-zero-overlap) is not sufficiently accurate, with relative error up to 17%. Moreover, the derivative of this analytical function is not continuous, which prevents accurate description of the force established within the comb. We have therefore proceeded in the behavior analysis with the capacitance description of the device based on FEM simulations. FEM data considers the contribution of the fringing electric fields more precisely and completely and offers a more accurate representation.

Furthermore, the fitting function facilitated the calculation of the capacitance derivative, allowing the deduction of the attractive electrostatic force $F_{el}(u) = \frac{1}{2}\frac{dC(u)}{du}V^2$ acting between the combs. The results in Fig. 2b indicate that the force, directly proportional to the capacitive gradient, remains at nearly constant values for $u/d < -5$ and $u/d > 3$, with a notable exception in an intermediate region where it undergoes rapid increase. We term this region, where the normalized overlap u/d ranges from -5 to 3, the *gray zone* (Fig. 2b). Within this zone, a

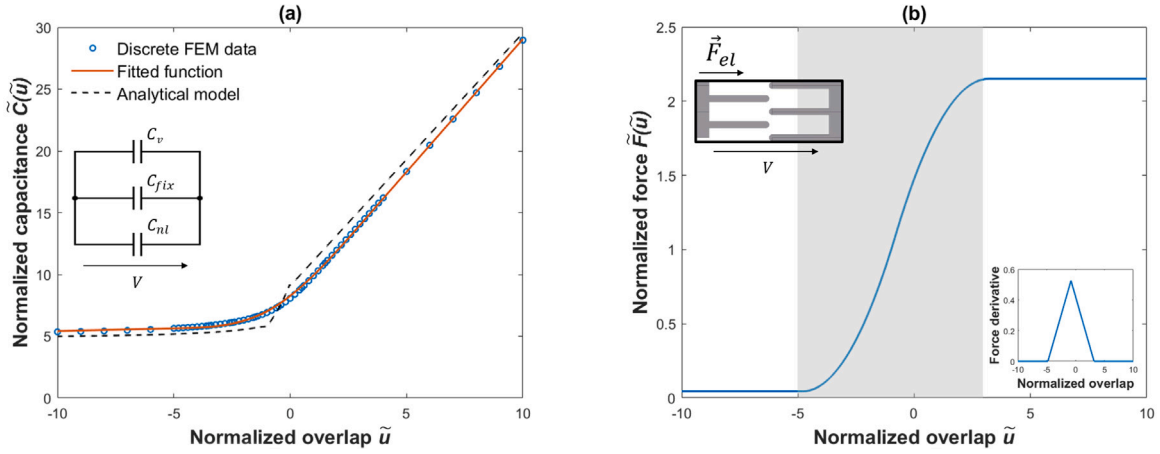

Fig. 2. Variation of the normalized (a) capacitance and (b) force (derived from the fitted capacitance curve) with respect to the overlap between the comb-drive fingers. Capacitance is normalized to $\epsilon_0 hN$, force to $\frac{1}{2}\frac{\epsilon_0 hN}{d}V^2$ and the overlap to finger width d. Capacitance has three different contributors: variable capacitance formed by the comb electrodes (overlap dependent), formed by the fixed electrode and substrate (constant across overlap range) and non-linear contributions like fringing fields.

significant force persists for negative overlaps due to the long-range influence of fringing electric fields. The structure also encounters the maximum force gradient within the gray zone. The effects of this force gradient, intricately linked to the second derivative of capacitance, will be discussed later.

In the following, we explore the practical implications of the earlier findings through an examination of a comb-drive actuator. In this experimental setup, the movable comb depicted in Fig. 1 is supported by a spring with a stiffness denoted as k. At the state of rest equilibrium, in the absence of both electrostatic and mechanical forces, we define u_0 as the initial overlap of the combs, a value predetermined by design. Upon the application of a voltage V, the attractive electrostatic force acting on the combs leads to an increase in overlap. Simultaneously, the spring force generated by the displacement tends to counteract the electrostatic force. The displacement x at equilibrium can be found by minimizing the potential energy E_p of the movable part of the system (Eq. (3)).

$$E_p = -\frac{C(u_0 + x)V^2}{2} + \frac{kx^2}{2} \tag{3}$$

As an illustration, we plot in Fig. 3 E_p versus x for $u_0 = 0$ and for a set of voltages V. The fitted function derived from the FEM calculation (red line in Fig. 2a) is used as $C(u)$ in this calculation. Results in Fig. 3 show that the higher the voltage V the higher the displacement x to reach the equilibrium state at the minimum of potential energy. The value of k used in simulation is 1.5 N/m.

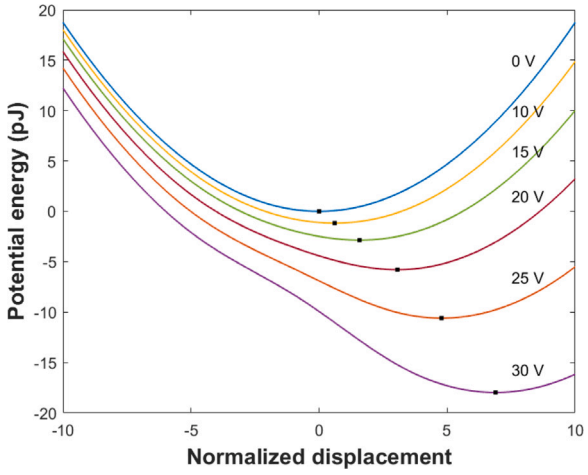

Fig. 3. Potential energy of the movable electrode for a set of voltages applied to the fixed electrode, keeping the movable electrode and the substrate grounded. Minimum values of the curves (black dots) correspond to the displacement x reached after application of the voltage V. See the text for further information.

3. Experimental characterization - DC displacement

In order to compare the model with experiments, we fabricated comb-drive actuators with three different initial overlaps $u_0 = -2d$, 0 and $2d$, d being the finger width (Refer to Appendix B for details on microfabrication process). The movable comb is suspended over a spring designed with a stiffness $k = 1.5$ N/m. The number of fingers in combs, their width, length and spacing was the same as described in Table 1 and used in the modeling. As for the characterization of these comb-drive actuators, we measured the displacement x of the movable part at equilibrium in response to a voltage V applied to the fixed comb, while grounding the substrate and the movable comb. Voltage V was increased in 0.5 V steps. We optically recorded the displacement of the shuttle using an optical camera (XIMEA xiQ). We performed image processing on the recorded frames and extracted the displacement with the accuracy of less than 50 nm. The measured values were compared to the expected equilibrium positions calculated from the potential energy, as described previously. Results are shown in Fig. 4.

For zero and positive initial overlaps u_0, Fig. 4a and b reveal a very good agreement between measurements and simulations. At first order, the displacement x versus the applied voltage V follows the expected quadratic trend typical of a conventional comb-drive actuator configuration. In contrast, Fig. 4c illustrates that for the negative initial overlap ($u_0 = -2d$), the measurement exhibits a steep increase as the displacement x exceeds 0.5 μm. Although the calculated displacement (solid line) also displays this steep increase, it is shifted in voltage compared to the experimental data. Further investigations involved the actuation of the device with forward and backward voltage sweeps. They reveal no hysteresis effect associated with the actuator displacement, thereby eliminating it as a potential explanation for the steep increase, as well as showing that there are no associated energy losses. Additionally, slight variations in the parameters of the structure were introduced in the FEM calculations of the capacitance in order to account for changes in dimensions resulting from the fabrication process during lithography and etching steps. These changes, particularly affecting

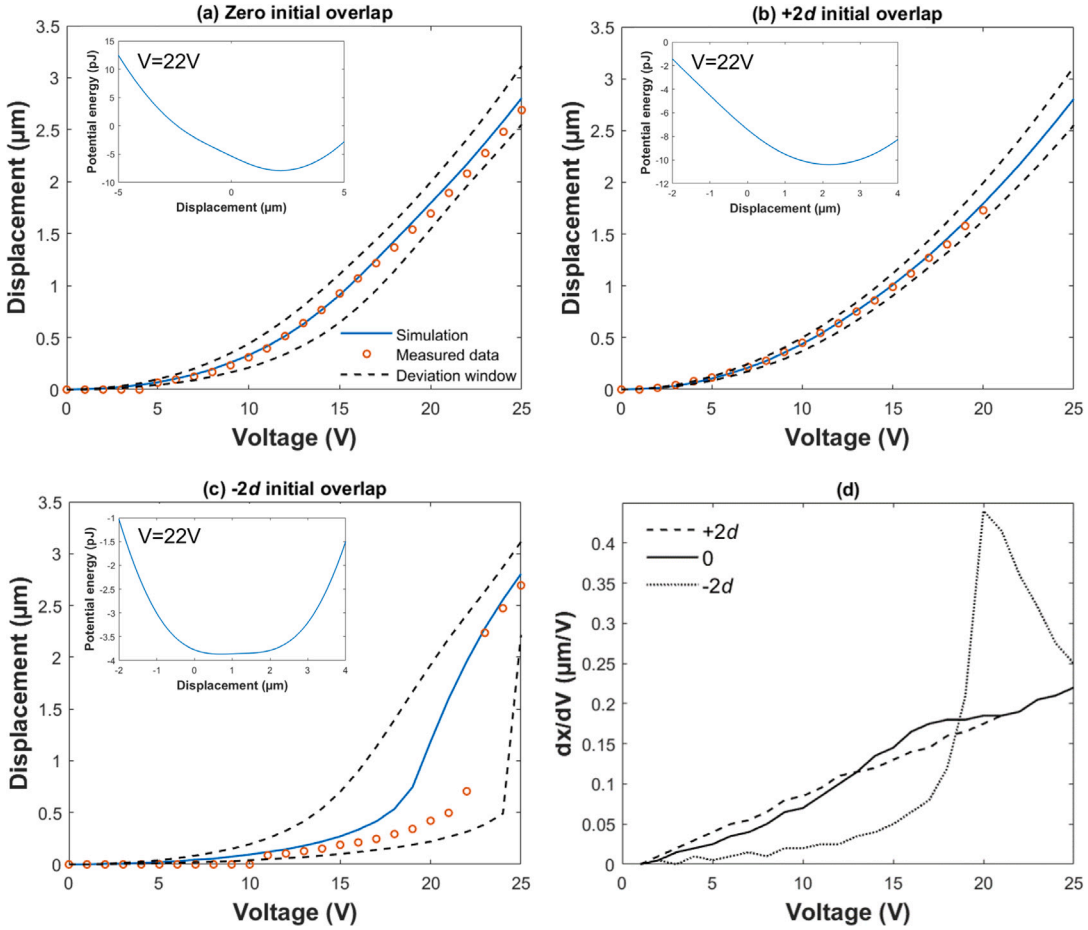

Fig. 4. (a)–(c): Comparison of the simulated (full line) and measured (circles) comb-displacement induced by applying a DC voltage on the fixed electrode, the movable electrode and the substrate being grounded for three different comb-drive configurations: (a) initial comb-overlap of 0, (b) 2*d*, and (c) −2*d*. The dashed lines represent the extreme variations of the geometrical parameters that can occur during device fabrication and they correspond to cases where finger length *l* and width of the structures are varied by 200 nm and 50 nm, respectively. (d) Derivative of displacement over voltage for three different initial overlaps, highlighting the highest sensitivity of the −2*d* geometry.

the length l of the fingers, the width d of the fingers and the width of the suspension beams (that spring constant k is highly dependent on), were incorporated. The corresponding displacement-voltage curves are represented by dashed lines in Fig. 4. Notably, for the negative initial overlap in Fig. 4c, the displacement-voltage characteristics are highly sensitive to these parameters. A change of less than 200 nm (2%) in the finger length and 50 nm in the width of the structures is sufficient to align the simulation with the experimental data. An interesting insight emerges in the inset of Fig. 4c, where the potential energy E_p versus displacement x is depicted at the actuation voltage $V = 22$ V corresponding to the steep increase. It highlights that the potential energy well remains flat over a span exceeding 1 μm. This explains why the displacement is extremely sensitive to the geometrical parameters governing the force balance of the comb-drive actuator with negative initial overlap. This observation also indicates that within this operation range, variations in the stored electrical and mechanical energies of the system offset each other, meaning that the electrostatic force gradient counterbalances the mechanical spring constant. This behavior is linked to the well-known electrostatic spring softening effect, resulting in the present case to a comb-drive actuator with a reduced apparent stiffness in the restricted region of the *gray zone*. This effect is also observable in Fig. 4d, where the displacement gradient over voltage for −2*d* initial overlap follows a steep increase within this region and reduces once outside of the *gray zone*. This could pave the way for actuators operating within the gray zone with an enhanced displacement-versus-voltage ratio and for force sensors with heightened sensitivity. In MEMS capacitive sensors, sensitivity is proportional to variation of capacitance caused by the displacement. In the case of a force sensor (e.g. an accelerometer), the displacement is caused by external forces acting on the mobile part of the sensor (e.g. the inertial force), meaning that the lower its stiffness, the larger the displacement, the greater the sensor sensitivity. In other words, the sensitivity of a force sensor is inversely proportional to its stiffness. As discussed previously, operation within the gray zone may significantly reduce apparent stiffness when the electrostatic spring constant counterbalances the mechanical spring constant of the comb-structure. Thus, we envision that a force sensor made of a comb-structure with negative initial overlap and adequately operated in the gray zone would experience significantly greater displacement for a given external force to sense. This would lead to enhanced sensitivity compared to an operation with engaged comb fingers.

4. Experimental characterization - AC vibration

The spring softening effect becomes further evident in the dynamic mode by examining the first resonance frequency f_r of the spring–mass system of the comb-drive actuator. When a voltage $V(t) = V_{DC} + V_{AC}\sqrt{2}\cos(2\pi f t)$ is applied to the device, the DC part induces a static displacement of the shuttle yielding an overlap u_{DC} of the comb fingers. Meanwhile, the AC part generates a time-varying force F_{AC} driving the

vibration at frequency f. The equation of motion in the dynamic mode is then expressed as Eq. (4):

$$m_{eff}\ddot{x} + \alpha\dot{x} + (k_{eff} + k_{el})x = F_{AC}(t) \tag{4}$$

where m_{eff} and k_{eff} denote the effective mass and spring constant of the system, respectively, and α represents the damping coefficient. x is the time-varying position of the shuttle with respect to the equilibrium position at overlap u_{DC}.

Assuming $V_{AC} \ll V_{DC}$, $F_{AC}(t)$ is expressed as $F_{AC}(t) = V_{DC}V_{AC}\sqrt{2}\frac{dC(u)}{du}\Big|_{u=u_{DC}}\cos(2\pi f t)$ and k_{el} as $k_{el} = -\frac{1}{2}V_{DC}^2\frac{d^2C(u)}{du^2}\Big|_{u=u_{DC}}$ (see details in Appendix C). k_{el} is the electrostatic spring constant arising from the second derivative of the capacitance at the overlap u_{DC}. The resonance frequency f_r is then calculated as:

$$f_r = \frac{1}{2\pi}\sqrt{\frac{k_{eff} + k_{el}}{m_{eff}}} \tag{5}$$

whereas the amplitude of the vibration at resonance is given by:

$$|x| = \frac{QF_{el}}{k_{eff}} = \frac{Q}{k_{eff}}V_{DC}V_{AC}\frac{dC(u)}{du}\Big|_{u=u_{DC}} \tag{6}$$

Practically, we measured the impedance of the comb-drive actuator versus frequency. The electrical response was then fitted with an $RLC–C_0$ circuit, allowing to deduce the resonance frequency f_r [20]. In Fig. 5a, f_r is plotted versus V_{DC} for a comb-drive actuator with zero initial overlap.

f_r exhibits variations greater than 10% towards low frequencies, indicating a substantial electrostatic spring constant k_{el} in the gray zone. Interestingly, a notable feature is observed in the measurements. Despite the quadratic dependence of k_{el} on V_{DC}, $|k_{el}|$ peaks at V_{DC} = 10 V and diminishes for larger voltages, leading in turn to an increase in f_r. This observation aligns with the evolution of capacitance: as V_{DC} increases, the overlap u_{DC} also increases, causing the capacitance to vary more linearly with displacement (see Fig. 2a), approaching the behavior of a comb-structure with engaged fingers. Consequently, the second derivative of capacitance tends towards 0 (as illustrated in the inset of Fig. 2b). Since $|k_{el}|$ is proportional to the second derivative of capacitance, it is also expected to decrease towards 0, as observed in Fig. 5a, resulting in the resonance frequency f_r tending to revert back to f_0. The difference in voltage values at which the maximum $|k_{el}|$ is observed between experimental measurements (V_{DC} = 10 V) and FEM simulations (V_{DC} = 13 V) can be explained by the device's high sensitivity to microfabrication process and geometric variations.

The vibration amplitude $|x|$ is represented in Fig. 5b in dependence on V_{DC} along with the static displacement u_{DC}. The vibration amplitude is also dependent on the amplitude of the AC voltage V_{AC}, as derived in the Eq. (6). The significant electrostatic spring constant within the *gray zone* could offer the possibility to design comb-drive micro-resonators capable of frequency tunability.

In this section, the dynamic mode was analyzed for small vibration amplitudes using the linear model given by Eq. (4). The description takes into account the non-linear variation of capacitance within the gray zone through the calculation of the electrostatic spring constant k_{el}. Higher-order non-linear terms could be introduced into the description, paving the way for an in-depth investigation of the non-linear dynamics of the system. This could potentially reveal a variety of complex behaviors like bifurcations and transitions between different coexisting response regimes, as has been widely studied in MEMS devices [21–23].

5. Conclusion

In conclusion, our study involved the capacitance modeling of comb-drive actuators, employing analytical and Finite Element Method (FEM) approaches, and particularly focusing on the unconventional regime where the fingers' overlap is close to zero and even negative. In this regime, fringing electric fields lead to a non-linear variation of the comb capacitance with the displacement. The electrostatic force is there rapidly varying, meaning that both first and second derivatives of the capacitance are significant. Consequently, these factors induce atypical behaviors in the comb-drive actuator across both DC and AC modes of operation. A notable outcome of our study was the discernible spring softening effect observed in the vicinity of near-zero overlap, resulting in peculiar characteristics in the displacement-voltage response. These results unveil new avenues for the development of sensors and actuators with enhanced sensitivity and for the realization of frequency-tunable microresonators. In AC mode, a substantial reduction in resonance frequency relative to the DC operating point was observed. This study contributes to the growing interest in comb-drive structures operating within the zero-overlap regime, with recent prospects including MEMS circuitry for adiabatic logic [16] and energy harvesting devices [11].

CRediT authorship contribution statement

A. Marković: Writing – original draft, Visualization, Software, Methodology, Investigation, Data curation, Conceptualization. **H. Fanet:** Conceptualization. **G. Pillonnet:** Writing – review & editing, Supervision, Funding acquisition, Conceptualization. **B. Legrand:** Writing – review & editing, Supervision, Conceptualization.

Declaration of competing interest

The authors declare that they have no known competing financial interests or personal relationships that could have appeared to influence the work reported in this paper.

Data availability

Data will be made available on request.

Funding

This work was supported by the French National Research Agency (ANR) under the research project Zerouate (grant ANR-19-CE24-0013) and by the RENATECH French national technological network.

Appendix A. Cubic Hermite spline interpolation

Starting from discrete Finite Element Method (FEM) data, we formulated a continuous function describing the variation of capacitance in relation to overlap u. This involved employing a cubic Hermite spline interpolator to effectively model the discrete FEM data. The overlap range was separated into four distinct regions, with each region i individually subjected to fitting via a third-degree polynomial of a form:

$$C_i(u) = a_i u^3 + b_i u^2 + c_i u + d_i \tag{A.1}$$

This method was employed to guarantee the continuity of both the fitting function and its derivative at the boundaries of the regions.

Appendix B. Microfabrication process

In this study, 4-inch (100 mm) (100) silicon-on-insulator (SOI) wafers were utilized, featuring a device layer with a thickness of 5 μm and a buried oxide layer with a thickness of 2 μm. The device layer exhibited a resistivity within the range of 0.001–0.005 ohm cm and was n-doped with arsenic (As) at a concentration ranging from 10^{19} to 10^{20} cm^{-3}. Prior to the commencement of the fabrication process, the wafers underwent a standard RCA cleaning procedure to ensure the elimination of all organic and ionic contaminants from the wafer surfaces.

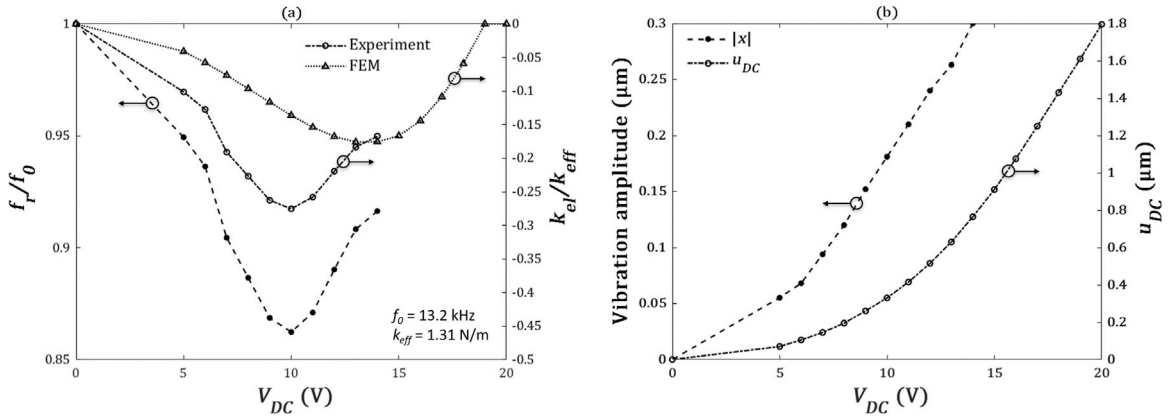

Fig. 5. (a) Variation of the resonance frequency f_r and of the electrostatic stiffness k_{el} of a comb-drive actuator measured for V_{DC} ranging from 5 to 14 V. Values marked with triangles are calculated from FEM data, the ones marked with circles are experimental. The resonance frequency f_0 = 13.20 kHz for V_{DC} = 0 V is extrapolated from the measurements (see Appendix D for details). k_{eff} = 1.31 N/m is the effective stiffness obtained assuming an effective mass of m_{eff} = 190 ng. The comb-drive actuator was designed and fabricated with a zero initial overlap. V_{AC} = 500 mV was used for the measurements. (b) Equilibrium position u_{DC} and the vibration amplitude |x| calculated for each of the DC voltages represented on the x-axis.

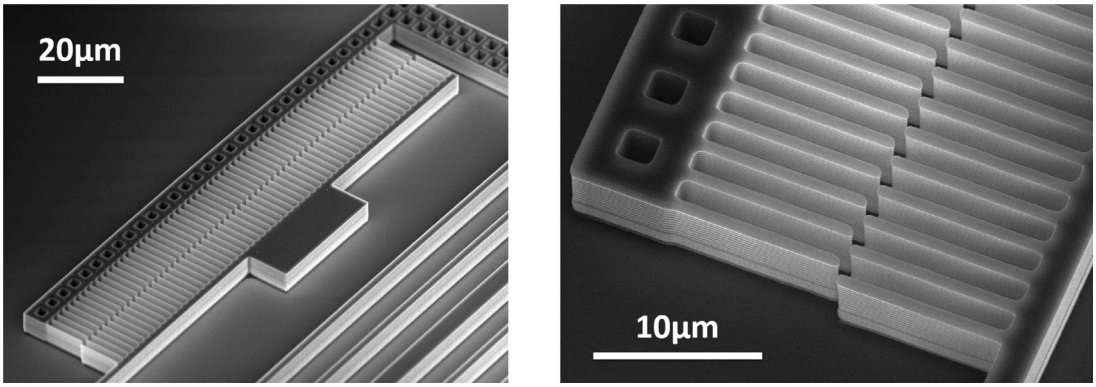

Fig. B.6. SEM images of a fabricated comb.

Subsequently, the cleaned wafers were coated with a bottom anti-reflective coating (BARC) and subjected to a baking process at 200 °C for 60 s. Following the cooldown of the BARC, a positive ECI (Micro-Chemicals) photoresist was applied, and a soft-baking step was carried out for 90 s using the EVG120 (EVG Group) automatic resist processing system. The exposure process was conducted using the Canon FPA 3000i4/i5 Stepper, allowing for photoresist exposure at 365 nm (i-line), followed by development in MF-CD-26 (Microposit) developer using the EVG120 system.

Pattern transfer into the silicon substrate was executed using the Alcatel AMS4200, a high-density plasma reactor, based on the inductively coupled plasma reactive ion etching (ICP-RIE) process. This reactor, designed for the treatment of 4-inch wafers, facilitated the etching of the top silicon layer through a deep reactive ion etching (DRIE) procedure, employing the Bosch process with a cycle of 2.2 s/2 s (SF_6/C_4F_8). Backside etching was strategically performed beneath unfixed device components to minimize parasitic capacitance.

Finally, movable parts were released through immersion in hydrofluoric acid, which selectively etched the buried oxide layer beneath the structures. The SEM image of a fabricated device is shown in Fig. B.6.

Appendix C. Calculation of F_{AC} and k_{el}

Equation of motion in the dynamic mode is given by:

$$m_{eff}\ddot{x} + \alpha\dot{x} + k_{eff}x = F_{el}(x,t) \tag{C.1}$$

where m_{eff}, x, α, k_{eff} and F_{el} represent the effective mass, the displacement with respect to the resting position (in the absence of voltage signals), damping coefficient, effective spring constant of the mechanical system and the electrostatic force, respectively.

The electrostatic force F_{el} within a comb-capacitor with a finger overlap u is given by

$$F_{el}(u,t) = \frac{1}{2}\frac{dC(u)}{du}V(t)^2 \tag{C.2}$$

Where V and C correspond to the voltage applied to the terminals and the comb-capacitance, respectively.

Around the equilibrium position u_{DC}, the position of the shuttle is $u = u_{DC} + x$, where u_{DC} is the overlap induced by V_{DC} and x is the time-varying position of the shuttle with respect to u_{DC}. Using Taylor expansion we can express comb-capacitance $C(u) = C(u_{DC} + x)$ as following:

$$C(u_{DC}+x) = C(u_{DC}) + \frac{dC(u)}{du}x\Big|_{u=u_{DC}} + \frac{1}{2}\frac{d^2C(u)}{du^2}x^2\Big|_{u=u_{DC}} + O(x^3) \tag{C.3}$$

This then gives us the electrostatic force in the form:

$$F_{el}(u_{DC}+x,t) = \frac{1}{2}V(t)^2\left[\frac{dC(u)}{du}\Big|_{u=u_{DC}} + \frac{d^2C(u)}{du^2}x\Big|_{u=u_{DC}} + O(x^2)\right] \tag{C.4}$$

Knowing that $V(t) = V_{DC} + V_{AC}\sqrt{2}\cos 2\pi f t$ and $V_{AC} \ll V_{DC}$, we can rewrite $F_{el}(t)$ as:

$$F_{el}(u_{DC}+x,t) = \frac{1}{2}\left[V_{DC}^2 + 2\sqrt{2}V_{DC}V_{AC}\cos 2\pi f t\right]\left[\frac{dC(u)}{du}\Big|_{u=u_{DC}} + \frac{d^2C(u)}{du^2}x\Big|_{u=u_{DC}}\right] \tag{C.5}$$

and by keeping only the terms at frequency f:

$$F_{el}(u_{DC}+x,t) = \sqrt{2}V_{DC}V_{AC}\cos 2\pi f t \frac{dC(u)}{du}\Big|_{u=u_{DC}} + \frac{1}{2}V_{DC}^2\frac{d^2C(u)}{du^2}x\Big|_{u=u_{DC}} \quad (C.6)$$
$$= F_{AC}(t) - k_{el}x$$

where $F_{AC}(t) = V_{DC}V_{AC}\sqrt{2}\frac{dC(u)}{du}\Big|_{u=u_{DC}}\cos 2\pi f t$ and $k_{el} = -\frac{1}{2}V_{DC}^2\frac{d^2C(u)}{du^2}\Big|_{u=u_{DC}}$.

Appendix D. Determination of f_0

The resonance frequency f_0 cannot be electrically measured since it occurs at $V_{DC} = 0$, where no oscillation amplitude is detectable. In this study, we estimated f_0 through data extrapolation. Our approach was as follows: We assumed that for V_{DC} voltages below 8 V, the static displacement u_{DC} is sufficiently small, allowing us to treat the second derivative of capacitance as constant. Additionally, we assumed that the electrostatic spring constant is negligible compared to the mechanical spring constant, enabling us to linearize Eq. (5). This approach results in a linear relationship between the resonance frequency and V_{DC}^2. With these assumptions in mind, and using the data points at V_{DC} = 5, 6, 7 and 8 V, we derived a fit to the data yielding f_0 = 13.2 kHz. This f_0 value was then utilized to generate Fig. 5a.

Appendix E. Supplementary data

Supplementary material related to this article can be found online at https://doi.org/10.1016/j.sna.2024.115652.

References

[1] R. Frank, Understanding Smart Sensors, Third ed, Artech House, Boston, MA, 2013.

[2] D.J. Bell, T.J. Lu, N.A. Fleck, S.M. Spearing, MEMS actuators and sensors: Observations on their performance and selection for purpose, J. Micromech. Microeng. 15 (7) (2005) S153, http://dx.doi.org/10.1088/0960-1317/15/7/022.

[3] J. Li, Q. Zhang, A. Liu, Advanced fiber optical switches using deep RIE (DRIE) fabrication, Sensors Actuators A 102 (3) (2003) 286–295, http://dx.doi.org/10.1016/S0924-4247(02)00401-6.

[4] M. Bao, Chapter 4 - electrostatic actuation, in: M. Bao (Ed.), Analysis and Design Principles of MEMS Devices, Elsevier Science, Amsterdam, 2005, pp. 175–212, http://dx.doi.org/10.1016/B978-044451616-9/50005-9.

[5] P.-F. Indermühle, V. Jaecklin, J. Brugger, C. Linder, N. de Rooij, M. Binggeli, AFM imaging with an xy-micropositioner with integrated tip, Sensors Actuators A 47 (1) (1995) 562–565, http://dx.doi.org/10.1016/0924-4247(94)00962-H.

[6] J. Dong, P.M. Ferreira, Electrostatically actuated cantilever with SOI-MEMS parallel kinematic XY stage, J. Microelectromech. Syst. 18 (3) (2009) 641–651, http://dx.doi.org/10.1109/JMEMS.2009.2020371.

[7] Z. Li, S. Gao, U. Brand, K. Hiller, H. Wolff, A MEMS nanoindenter with an integrated AFM cantilever gripper for nanomechanical characterization of compliant materials, Nanotechnology 31 (30) (2020) 305502, http://dx.doi.org/10.1088/1361-6528/ab88ed.

[8] P. Li, T. Sasaki, L. Pan, K. Hane, Comb-drive tracking and focusing lens actuators integrated on a silicon-on-insulator wafer, Opt. Express 20 (1) (2012) 627–634, http://dx.doi.org/10.1364/OE.20.000627.

[9] C. Yamahata, D. Collard, B. Legrand, T. Takekawa, M. Kumemura, G. Hashiguchi, H. Fujita, Silicon nanotweezers with subnanometer resolution for the micromanipulation of biomolecules, J. Microelectromech. Syst. 17 (3) (2008) 623–631, http://dx.doi.org/10.1109/JMEMS.2008.922080.

[10] J. Bernstein, S. Cho, A. King, A. Kourepenis, P. Maciel, M. Weinberg, A micromachined comb-drive tuning fork rate gyroscope, in: [1993] Proceedings IEEE Micro Electro Mechanical Systems, 1993, pp. 143–148, http://dx.doi.org/10.1109/MEMSYS.1993.296932.

[11] B. Vysotskyi, J.-F. Ambia Campos, E. Lefeuvre, A. Brenes, Dynamic analysis of a novel two-sided nonlinear MEMS electrostatic energy harvester, Mech. Syst. Signal Process. 206 (2024) 110932, http://dx.doi.org/10.1016/j.ymssp.2023.110932.

[12] W.C. Tang, T.-C.H. Nguyen, R.T. Howe, Laterally driven polysilicon resonant microstructures, in: IEEE Micro Electro Mechanical Systems, Proceedings, 'An Investigation of Micro Structures, Sensors, Actuators, Machines and Robots', 1989, pp. 53–59.

[13] S.D. Senturia, Microsystem design, in: Microsystem Design, First ed, Springer, New York, NY, 2013, http://dx.doi.org/10.1007/b117574.

[14] Y. Perrin, A. Galisultanov, L. Hutin, P. Basset, H. Fanet, G. Pillonnet, Contact-free MEMS devices for reliable and low-power logic operations, IEEE Trans. Electron Devices 68 (6) (2021) 2938–2943, http://dx.doi.org/10.1109/TED.2021.3070844.

[15] G. Pillonnet, H. Fanet, S. Houri, Adiabatic capacitive logic: A paradigm for low-power logic, ISCAS, in: 2017 IEEE International Symposium on Circuits and Systems, IEEE, Baltimore, United States, 2017, pp. 1–4, http://dx.doi.org/10.1109/ISCAS.2017.8050996.

[16] A. Marković, L. Mazenq, A. Laborde, H. Fanet, G. Pillonnet, B. Legrand, Ultra-low-power logic with contactless capacitive MEMS, in: 2022 21st International Conference on Micro and Nanotechnology for Power Generation and Energy Conversion Applications, PowerMEMS, IEEE, 2022, pp. 223–227.

[17] W. Zhao, X. Li, S. Gu, S.H. Kang, M.M. Nowak, Y. Cao, Field-based capacitance modeling for sub-65-nm on-chip interconnect, IEEE Trans. Electron Devices 56 (2009) 1862–1872, http://dx.doi.org/10.1109/TED.2009.2026162.

[18] W. Tan, X. Margueron, An Improved Parasitic Capacitance Cancellation Method for Planar Differential Mode Inductor in EMI Filters.

[19] J. D'Errico, SLM - shape language modeling, 2024, MATLAB Central File Exchange, URL https://www.mathworks.com/matlabcentral/fileexchange/24443-slm-shape-language-modeling.

[20] G.K. Feder, Chapter 6 – capacitive resonators, in: B. Oliver, D. Isabelle, H.S. M., J. Fabien (Eds.), Resonant MEMS, First ed, Wiley-VCH, Weinheim, 2015, pp. 121–146.

[21] J.F. Rhoads, S.W. Shaw, K.L. Turner, Nonlinear Dynamics and Its Applications in Micro- and Nanoresonators, J. Dyn. Syst. Meas. Control 132 (3) (2010) 034001, http://dx.doi.org/10.1115/1.4001333.

[22] M.C.C. Ron Lifshitz, Nonlinear dynamics of nanomechanical and micromechanical resonators, in: Reviews of Nonlinear Dynamics and Complexity - Chapter 1, Wiley-VCH Verlag GmbH & Co. KGaA, 2008, http://dx.doi.org/10.1002/9783527626359.

[23] S. Tiwari, R.N. Candler, Using flexural MEMS to study and exploit nonlinearities: A review, J. Micromech. Microeng. 29 (2019) 083002, http://dx.doi.org/10.1088/1361-6439/ab23e2.

Aleksandra Marković was born in Belgrade, Serbia in 1993. She obtained her Bachelor's degree in Electrical Engineering from TU Vienna, Austria in 2016 and Master's degree in Microengineering from EPFL, Switzerland in 2019. After spending one year at Harvard University as a visiting student, she joined LAAS-CNRS as a Ph.D. candidate in 2021. She is currently working on ultra-low-power logic gates based on capacitive MEMS devices operating in adiabatic regime.

Hervé Fanet received in 1971 the engineer's diploma from the "Ecole Supérieure d'Electricité". He was involved in detectors and electronic developments for high energy particle Physics. He joined CEA-LETI in 1996 and was in charge of medical imaging research and manager of integrated circuits design department. His current research topics include smart sensors and ultra-low power electronics. He has published 40 papers in journals and is author or co-author of five books.

Gaël Pillonnet received his Master's degree in Electrical Engineering from CPE Lyon, France, in 2004, a Ph.D. and habilitation degrees from INSA Lyon, France in 2007 and 2016, respectively. Following an early experience as analog designer in STMicroelectronics in 2008, he joined the University of Lyon as associate Professor. During the 2011-12 academic year, he held a visiting researcher position at the University of California at Berkeley. Since 2013, he is in CEA-Léti, Grenoble, France, involved in developing various projects in design technology co-optimization. During the 2022–2023 academic year, he joins energy-efficient microsystems group at UCSD as a visiting researcher. He is now the scientific advisor for the Silicon component division in CEA-Léti. His research focuses on power-conversion oriented circuits such as DC-DC converters, audio amplifiers, adiabatic logics, electromechanical transducers, harvesting electrical interfaces. He is also involved in various device/circuit design enablement for RRAM, Si-qubit, solid-state energy storage and MEMS sensors.

Bernard Legrand received the electrical engineering degree and the M.S. degree in electronics in 1996, and the Ph. D. degree in electronics in 2000 from the Université des Sciences et Technologies de Lille, Villeneuve d'Ascq, France. He was appointed a CNRS research scientist in 2001 and joined the Silicon Microsystems Group of IEMN, Lille, France. In 2013, he moved to the LAAS-CNRS in Toulouse, France, where he headed the Micro-Nano-Bio-Technologies department from 2015 to 2021. From 1996 to 2000, he worked on semiconductor nanostructures, including fabrication and characterization. Since then, his research topics have covered MEMS devices and their applications, with a particular interest for the electromechanical transduction and for resonant sensors. He served as a member of technical program committees of international conferences in the field, including IEEE MEMS and IEEE IEDM.